

Analysis of diverting and focusing flow in unsaturated fractured tuffs at Yucca Mountain,
Nevada.

Lehua Pan, Yu-Shu Wu, and Keni Zhang

Earth Sciences Division

Lawrence Berkeley National Laboratory

Berkeley, CA 94720

November 2001

Prepared for *Vadose Zone Journal*

LBL-49274

1. **Introduction**

Diversion and focusing of water flow in the vadose zone occurs in many natural subsurface systems and is of great importance in many scientific and engineering fields. The major factor controlling such diversion and focusing is the spatial distribution of the flow-barrier (e.g., capillary-barrier formed at the contact interfaces between the strata of different soils and rocks with contrasting hydrological properties). In general, there exists lateral heterogeneity even with layered formations at an actual site. For example, a fault system, if present, could alter the spatial distribution of such barriers by breaking the continuity of those barriers as well as creating new barriers through both displacement of the strata of rocks and altering the hydrological properties of the hosting rocks. In a vadose zone of fractured rocks, the existing of fractures with varying intensity in different strata of rocks could further complicate the formation and distribution of these barriers. As a result, locally saturated regions, lateral water movement, and focusing of downward flow may develop in the vadose zone and lead to a complicated flow pattern that would not occur in an otherwise uniform vadose zone.

The thick unsaturated zone (UZ) at Yucca Mountain, Nevada, the site currently under consideration by the U.S. Department of Energy as a potential repository site for the storage of high-level radioactive waste, is such a complex vadose zone. Understanding of flow pattern in the UZ of Yucca Mountain is essential in assessing the performance of the potential repository and helps the design of the potential repository. During early site characterization of the UZ at Yucca Mountain, the capillary-barrier and lateral flow concept was proposed and studied conceptually (Montazar and Wilson, 1984).

Subsequent numerical models (Rulon et al., 1986; Wittwer et al., 1995; Moyer et al., 1996; Wu et al., 1998; Wu et al., 1999; Wu et al., 2000) have shown a wide range of variability in the amount of lateral flow caused by the capillary-barriers or permeability-barriers in fractured tuffs, using various grid resolutions and supporting field data. A systematic analysis of the flow diversion and focusing caused by the flow-barriers in the UZ at Yucca Mountain is deemed necessary and important in both understanding the water flow regime in the vadose zone and evaluating the performance of the potential repository.

Problems with sloping, layered soils were addressed by Zaslavsky and Sinai (1981a, b). During the last few decades, quantitative analyses of water flow in layered porous media were presented, mainly for capillary-barriers (Miyazaki, 1988; Ross, 1990, 1991; Steenhuis et al., 1991; Fayer et al., 1992; Oldenburg and Pruess, 1993; Yeh et al., 1994; Stormont, 1995; Morel-Seytoux et al., 1996; Wilson 1996; Warrick et al., 1997; Pan et al., 1997; Webb, 1997; Ho and Webb, 1998; Morel-Seytoux and Nimmo, 1999). Most investigations have focused on analytical or numerical analyses of the flow diversion as the effects of either a single capillary-barrier at the layer contact interface or multiple but parallel substrata interfaces (parallel to the surface). Systematic analysis of 3-D flow diversion and focusing in a vadose zone due to flow-barriers is rare in literature. Understanding of the interactions between the barriers that are non-parallel or intersected remains poor. Very few studies have been conducted and reported in the literature regarding the roles of the fractures in forming the flow-barriers (Wu et al., 2000).

The objective of the present study is to systematically analyze the flow diversion and focusing caused by the complicated flow-barrier system in the UZ at Yucca Mountain. In particular we will analyze (1) the role of fractures in forming and destruction of the flow barrier, (2) possible large-scale lateral flow, (3) the effects of faults on the configuration of the overall flow pattern. We also present the new extension to the analytical solutions of Warrick et al. (1997) and include layers consisting of fractured rocks using an effective continuum model (ECM) rather than single-porosity soils. The emphasis is on steady-state flow under ambient conditions.

2. Hydrogeological conditions

As shown in Figure 1, the domain of the UZ model encompasses approximately 40 km² of the Yucca Mountain area [*Hinds and Pan*, 2000; *Wu et al.*, 2000]. Vertically, the UZ is between 500 and 700 m thick, and overlies a relatively flat water table in the vicinity of the potential repository area. The potential repository would be located in the highly fractured Topopah Spring Tuff, approximately 200 m or more above the water table.

The net infiltration rate at the bedrock surface varies spatially from 0 to 15 mm/yr with an average value (over the domain) of 4.56 mm/yr. Figure 2 shows the spatial distribution of the net infiltration. Higher infiltration rates mainly occur in the northern part of the model domain and along the mountain ridge east of the Solitario Canyon fault from south to north. The net infiltration rate is below 4 mm/yr in the majority of the model domain, and the low water recharge provides one of necessary conditions for development of a thick vadose zone as well as formation of the capillary-barriers in the area.

The UZ at Yucca Mountain consists of alternating layers of welded and nonwelded ash-flow and air-fall tuffs. Based roughly on the degree of welding, the geological formations have been divided into five major hydrogeologic units (Montazer and Wilson, 1984): the Tiva Canyon welded (TCw), the Paintbrush nonwelded (PTn), the Topopah Spring welded (TSw), the Calico Hills nonwelded (CHn), and the Crater Flat undifferentiated units. Each major unit has been further divided into subunits in UZ flow model (Hinds and Pan, 2001) mainly based on the rock matrix properties provided by Flint (1998) and other updated geological information in current Geologic Framework Model of Yucca Mountain (GFM 3.1, Clayton, 2000). These layers of rocks generally are dipping to the east at about ten degrees or less (Figure 3). They also vary significantly in thickness over the model domain and some layers may even completely missing (pinched out) in some locations. The general trend is thinning to the south, especially in the northern part (Figure 4). As a result, the layer contacts are generally dipping to the east or south-east (northern part) but are not parallel to the bedrock surface or one another (Figures 3 and 4). Furthermore, the dipping degree can also vary significantly in both cross sections.

Faults at Yucca Mountain can significantly alter the hosting rock properties (Montazar and Wilson, 1984; Day et al., 1998) and discontinue the layers by displacement of geological formations (e.g., Solitario Canyon Fault). Therefore, vertical capillary-barriers may form along the faults and intersect the possible lateral capillary-barriers. On the other hand, the high permeability in the fault zone could facilitate rapid vertical drainage of the water accumulated by capillary diversion.

3. Theory and method

Mechanisms of flow diversion and focusing

Infiltrating water can be diverted by various barriers and tends to flow through the media where the resistance is smaller than others in a heterogeneous vadose zone. Under steady-state flow condition, such barriers and high conductive paths can be described by the spatial distribution of the effective hydraulic conductivity. Because the effective hydraulic conductivity is a function of water potential in the media, the spatial configuration of these barriers and high conductive paths for a given vadose zone also depends on the infiltration rate.

In the UZ of the Yucca Mountain, the main mechanism of forming flow barriers is the existing of dipping interfaces of tuffs where a high conductive tuff overlays a lower conductive tuff under certain conditions. For example, when PTn21 overlays PTn22, the interface between them could be a barrier to the downward infiltration water if the capillary pressure head at the interface corresponding to a given infiltration rate is -10 m or below. As shown in Figure 5, the hydraulic conductivity in PTn21 is about 300 times of that in PTn22 at $h = -10$ m. As a result, the water will build up above the interface and down-dip movement of the moisture occurs within the higher conductive PTn21. The lateral flow or flow diversion can take place in a large scale if such a barrier is maintained so. When the local capillary pressure head increases to certain degree (e.g., above -0.5 m for PTn21/PTn22 interface), however, the barrier will diminish and the lateral flow will cease. The downward flow through such leakage areas will have a rate significantly greater than the average infiltration rate because of receiving the moisture

diverted from neighboring areas. In other words, flow focusing occurs due to forming and diminishing of the capillary barriers spatially.

Three mechanisms may cause forming of such leakage areas:

1. The layer continuity is disrupted by a fault so that the local conditions for forming the capillary barrier is eliminated. For example, the down-dip flow within the PTn21 will be stopped at the front of a fault because the corresponding hydraulic conductivity in the fault zone (PTnFL in Figure 5) is as low as that of the PTn22. This will cause the moisture built up and drive the local water pressure head up to such a point that the capillary barrier diminished. Note that the leakage area will form right outside of the fault zone because the hydraulic conductivity of PTn22 increases faster and crosses over that of PTn21 earlier than that of PTnFL as the water pressure head increases. In other words, the focused downward flow paths are along the fault zone but outside of the fault zone. In case that the fault did not alter hosting rock properties significantly, the displacement of geological layers due to fault offsets could also cause the similar phenomena.
2. The thickness of the critical layer decreases to a limiting value or even it completely pinches out so that the capillary barrier is removed from such a region. The critical layer could be either the low conductive layer (e.g., PTn22) or the high conductive layer (e.g., PTn21). If PTn22 pinches out somewhere, the capillary barrier diminishes there too because the underlain layer becomes PTn23 which has similar hydraulic conductivity of PTn21. If PTn21 pinches out somewhere, the down-dip flow will be stopped there in a way similar to the case

of fault interruption. The difference is that the lateral barrier is formed by TCw13 that has even lower hydraulic conductivity than PTnFL corresponding to the interesting water pressure head range. As a result, the moisture will build up there and the focused downward flow path occurs there. Furthermore, even if the high conductive layer does not pinch out, the local capillary barrier can be possibly removed just because the thickness of the high conductive layer (e.g., PTn21) reduced to such a value that the down-dip flow feels a significant resistance. As a result, the moisture builds up to a level that the hydraulic conductivity of PTn22 becomes close to or larger than that of PTn21 at that localized region.

3. Change of dipping angles of the layer contacts, especially merging together of two opposite-dipping layer contacts, could also remove the capillary barrier in the merging area and cause to form a focused downward flow path. In Yucca Mountain, such layering structures can be seen clearly in the North-south direction (Figure 4) where the thickness of “PTn” significantly becomes thinner to the south and the top of “TSw” dips to the north in south region and to the south in the north region.

Analytical analysis

Assuming a local thermodynamic or capillary equilibrium condition between fracture and matrix continua, the effective continuum method (ECM) can be used to describe unsaturated flow in fractured rocks. Under such a flow condition, the Richards' equation can be written in the same form as for flow in a single-continuum porous medium in terms of the ECM formulation [Wu, 2000]. In particular, for steady-state percolation in a

vadose zone of dipping and parallel layers, it can be written as (pseudo one-dimensional flow) [Philip, 1991]:

$$\frac{\partial}{\partial n} \left[K(h) \frac{\partial h}{\partial n} \right] + \frac{\partial K(h)}{\partial n} \cos(\beta) = 0 \quad (1)$$

where, h , n , and β are capillary pressure head, the normal coordinate, and the angle of the layer interface, respectively. Note that n is measured upwards and perpendicular to the interface. $K(h)$ is effective hydraulic conductivity, as a function of capillary pressure.

$$K(h) = K_{f,s} k_{rf}(h) + K_{m,s} k_{rm}(h) \quad (2)$$

where $K_{f,s}$ and $K_{m,s}$ are saturated hydraulic conductivity of fracture and matrix continua, respectively while k_{rf} and k_{rm} are the relative permeability to water for fracture and matrix continua. Note that under the capillary equilibrium assumption, pressure heads in fractures and matrix are the same locally

In the ECM formulation, the problem, as described by Equation (1), for flow through unsaturated fractured rocks, becomes equivalent to that through porous soils [Warrick *et al.*, 1997]. Therefore, the analytical solutions derived by Warrick *et al.* [1997] may be directly extended to the case of fractured media using the ECM approximation. The pressure profile for a vadose zone of p parallel layers is then described by

$$(n - n_{i-1}) \cos(\beta) = \int_{h_{i-1}^*}^h \frac{dh}{\frac{q}{K_i(h)} - 1} \quad n < n_i, \quad i = 2, 3, \dots, p \quad (3)$$

where $h_1^* = h_1$, the pressure head in the first layer (the lowest layer), which is subject to the condition $K_1(h_1) = q$. $K_i(h)$ is the effective hydraulic conductivity of the i th layer and q is the infiltration rate. The total horizontal flow Q_h can be calculated as

$$Q_h = -\tan(\beta) \sum_{i=2}^p \int_{h_{i-1}^*}^{h_i^*} K_i(h) dh \quad (4)$$

Note that these results do not depend on any particular form of hydraulic conductivity $K(h)$ relationships. In the following study, the van Genuchten functions (van Genuchten, 1980) are used to describe both fracture and matrix continua.

Numerical analysis

The numerical analyses presented in this study were carried out using the unsaturated flow module of TOUGH2 family of codes (Pruess, 1991; Wu et al., 2001). The numerical scheme of the TOUGH2 family of codes is based on the integral finite-difference method to solve the Richards' equation. Because both matrix-matrix flow and fracture-fracture flow are considered important (Wu et al., 1999), the dual-permeability model is used to represent the fractured porous media. In the dual-permeability model, the formation domain is represented by two overlapping (yet interacting) fracture and matrix continua. The traditional approximation of fracture-matrix flow (Warren and Root, 1963) is used

but modified using an active-fracture model (Liu et al., 1998) to incorporate fingering flow effects through fractures. The resulting discretized finite-difference equations are highly nonlinear and are solved using the Newton/Raphson iterative scheme.

For 2-D numerical analyses, the horizontal spacing (Δx) is 10 m for both the east-west cross section W-E' (Figure 6) and the N-S cross section (Figure 7) (See Figure 1 for the two cross-section locations). The vertical resolution varies between layers based on the importance and thickness of a particular layer. The maximum Δz in the grids is between 2 and 20 m for the east-west cross section and between 2 and 4 m for the north-south cross section, respectively. For 3-D, site-scale numerical analysis, the maximum Δz varies between layers (3.5 – 69 m). The map view of the 3-D grid is shown in Figure 8. The resulted dual-permeability grid consists of 1,077,522 grid cells and 4,047,209 connections.

4. Results and discussions

Analytical analysis

Analytical solutions are useful for describing the fundamental characteristics of the capillary barrier system even though they rely on idealization of complicated subsurface flow processes. We will use analytical solutions for identifying layer contacts that may act as capillary barriers in the unsaturated zone of Yucca Mountain under ambient infiltration, evaluating the potential capillary-barrier diversion length responding to various infiltration rate, and assessing the roles of fractures in forming capillary barriers.

Because there are significant differences in the layer thickness and hydraulic properties between the northern part and the southern part of the Yucca Mountain, we select two representative layer combinations, based on data found at boreholes UZ-14 (representing the northern part) and SD-12 (representing the southern part). The profile at UZ-14 extends from the elevation of 1341.1m (top of PTn21) down to the elevation of 667.5m (bottom of bf3), while the profile at SD-12 extends from the elevation of 1322.1m (top of TCw12) down to an elevation of 660.5m (bottom of bf3). A dipping angle of 10 degrees is used to catch the upper bound of the potential capillary-barrier effects.

The analytical analysis shows that the capillary-barrier-diverted flow of the entire profile is contributed only by a few critical layers in both profiles and varies with the infiltration rate. However, the spatial distribution of the flow diversion between layers depends significantly on the particular layering structure and infiltration rates.

In the profile of UZ-14, the five critical layers (based on the magnitude of each layer) are PTn23, PTn21, PTn25, Pp1, and TSw32, listed in the order of their relative contributions to the total horizontal flow of 8.20 m²/yr corresponding to a infiltration rate of 5 mm/yr (Table 1). The capillary-barrier diversion length of the entire profile (i.e., the ratio of the total horizontal flow rate to the infiltration rate) is 1639.09 m. The total horizontal flow of the entire profile is calculated as the algebraic summation over all layers, while the up-slope horizontal flow (i.e., negative Q_h) takes place in certain layers but with much smaller magnitudes than the down-dip flow. These five layers conducts more than 99.99% of the total horizontal flow of the entire profile. Among them, PTn23 with a

thickness of 3.9 m conducts 88% of the total horizontal flow, and the PTn23/PTn24 contact is found to be the most important capillary barrier in the profile. Figure 9a shows a profile of the effective hydraulic conductivity corresponding to the infiltration rate of 5 mm/yr. As shown in the figure, there is a base value of the hydraulic conductivity (i.e., the value of the infiltration rate), companioned by many jumps in the hydraulic conductivity when crossing contact of different rocks. Because the hydraulic conductivity is a monotonic function of water pressure head within each layer, a positive jump of the hydraulic conductivity in the profile (i.e., jump above the base value) indicates a positive horizontal flow (i.e., down-dip flow) according to Equation (4). The five critical layers listed in Table 1 are corresponding to five major positive jumps in Figure 9a. For the case of an infiltration rate of 1000 mm/yr, the total horizontal flow of the entire profile increases to 65.97 m²/yr but the capillary diversion length decreases to 65.97 m. Distribution of the capillary-barrier diversion flow changes tremendously too. Now, TSw31 with a thickness of 2 m becomes the most important layer and conducts about 63% of the total horizontal flow of the entire profile (Table 1). The most critical layer PTn23 for an infiltration rate of 5 mm/yr becomes secondary in the case of an infiltration rate of 1000 mm/yr and contributes only less than half of that by TSw31. Figure 9b shows the corresponding distribution of the effective hydraulic conductivity. Obviously, the wetter condition significantly increases the heights of the jumps at the TSw31/TSw32 contact and decreases those at the PTn23/PTn24 and PTn21/PTn22 layer contacts (Figure 9a and 9b). As a result, the relative importance of these layers on the overall capillary-barrier effects also changed responding to different infiltration rates. Although the total contribution of the five most critical layers in the wet case just decreases slightly (to

99.73%), the horizontal flow is more evenly distributed among these critical layers in the wet case ($q = 1000 \text{ mm/yr}$) than in the dry case ($q = 5 \text{ mm/yr}$).

The capillary-barrier effect in the southern part (represented by the SD-12 profile) is weaker than in the northern part (represented by the UZ-14 profile) for the same dipping angle and infiltration rate of 5 mm/yr . The total horizontal flow of the entire profile is $6.72 \text{ m}^2/\text{yr}$ and the corresponding capillary diversion length is 1344.8 m (Table 2).

However the trend is opposite in the wet condition. The total horizontal flow is $105.73 \text{ m}^2/\text{yr}$ and the corresponding capillary diversion length is 105.73 m . In other words, the capillary-diversion lengths in the SD-12 profile are 82% (dry condition) and 160% (wet condition) of those in the UZ-14 profile, respectively. The reason is the difference in composition of the most critical layers within two profiles. The most critical layer in the UZ-14 profile, PTn23, becomes pinched out in the SD-12 profile and the zeolitic rocks of the Calico Hills formation in the UZ-14 profile turns into vitric in the SD-12 profile. As a result, in the dry condition, PTn21 becomes the most important layer and conducts about 46% of the total horizontal flow (i.e., the algebraic summation over all layers). Notably, Ch1 with a thickness of 22.5 m and Ch5 with a thickness of 14.3 m together conduct about 54% of the total horizontal flow, while they are insignificant in conducting lateral flow in the UZ-14 profile because of very low permeability due to higher zeolite abundance (Table 2). In the wet condition, Ch1 becomes the most important layer and conducts about 42% of the total horizontal flow. Like that in the UZ-14 profile, TSw31 exceeds PTn21 in conducting lateral flow (Table 2). Different from the situation in the UZ-14 profile, only about 50% or less of the down-dipping diversion flow takes place at

elevations above the potential repository horizon (mostly in TSw35) in the SD-12 profile (Table 1 and 2). Figure 10 shows the distribution of the effective hydraulic conductivity in the SD-12 profile.

To show the effects of fractures, we construct the same profiles with matrix only. Figure 11 shows the water pressure head distributions responding to an infiltration rate of 5 mm/yr. Both profiles become saturated above the layer of Pp4 (at elevation of 815.2 m at UZ-14 and 821.3 m at SD-12) for an infiltration rate of 5 mm/yr because Pp4 has very low saturated hydraulic conductivity (1.484 mm/yr). Because the zeolitic layers of the Calico Hills formation in UZ-14 profile also have very low saturated hydraulic conductivity (0.068 - 2.1 mm/yr), the second jump in water pressure head occurs at the top of Ch1 (at elevation of 927.2 m). In the SD-12 profile, the largest jump in the water pressure head occurs within TCw12 (this layer was eroded in the UZ-14 profile) because of its very low saturated hydraulic conductivity (about 0.095 mm/yr). Although the actual net infiltration rate could be lower if there were no fractures in the profiles, the existence of fractures is essential in draining the unsaturated zone of the Yucca Mountain. In other words, if there were no fractures, the deep unsaturated zone (about 700 m) in the Yucca Mountain would not exist.

On the other aspect, the diversion length would greatly increase to 278463.0 and 410948.1 m for UZ-14 and SD-12 profiles, respectively. However, such flow diversion is not due to the capillary barrier but due to the permeability barriers created by layers with very low saturated hydraulic conductivity. As a result, some layer (e.g., PTn22) in the

capillary barrier cases becomes the conducting layer in these non-capillary barrier cases because of its higher saturated hydraulic conductivity (Table 3).

Numerical analysis

Numerical modeling can be used to analyze more complicated flow diversion and focusing systems than those analytical approaches can. We will analyze the detailed structures of the flow diversion/focusing systems with two 2-D cross section simulations and the overall percolation patterns in the Yucca Mountain with a full 3-D, site-scale model. In particular, we will focus on those phenomena and factors that cannot be analyzed using an analytical approach, including the interactions between capillary barriers with different dipping angles or different geological composition, the effect of the spatial variable thickness of the critical layers, the flow focusing, and the role of fractures in forming and destroying capillary barriers. To minimize the grid discretization errors, finer vertical resolutions (Δz) were used for the critical layers revealed in the analytical analyses above.

Because the mass flux varies by orders in magnitude, it is hard to plot the flow field using a vector plot. As alternative, we plot the magnitude of numerically simulated 2-D vectors of mass flux along the east-west cross section (through UZ-14) under uniform surface infiltration (5 mm/yr) in Figure 12. The flow directions can be easily identified based on the continuity of the mass flux. In TCw formation, flow is downward dominant with a magnitude comparable with the uniform infiltration rate. The small spatial variation in the magnitude of the mass flux is mainly due to the effect of the landscape.

The two laterally continuous zones of high flux (about 6 times of the infiltration rate in magnitude) are PTn21 and PTn23, respectively. This result is consistent with the results of the analytical analysis that PTn23 and PTn21 conduct more than 99% of the total horizontal flow (Table 1). Two underlying layers, PTn22 and PTn24, act as the capillary barriers here because their lower effective hydraulic conductivity at that capillary pressure (Figure 5). Below PTn24, the flux becomes very small in magnitude because the infiltration water is diverted to the down ends of the capillary barriers, except several local regions where the capillary barriers diminished. The lateral high flux zones can extend beyond 1000 m and are usually stopped by faults. The faults with altered hydraulic properties from the host rocks become vertical capillary barriers. These vertical capillary barriers halt the lateral down-dip flow and the moisture builds up in these intersection regions as a result. Because the hydraulic conductivity in the fault-altered PTns increases slower than that in the normal PTns with the increase of water pressure (Figure 5), the moisture will breakthrough the capillary barriers consisting of PTn22 or PTn24 before it can overcome the vertical barriers of the faults. As a result, the vertical fast flow paths form along the faults (Figure 12). For the same reason, the vertical fast flow paths smear towards west on the way down. In such vertical fast flow paths, the flux can be above 6 times of the infiltration rate in magnitude on average for the given ambient condition. Clearly, such flow focusing phenomena are results of combined effects of two types of capillary barriers. Figure 13 shows that the vertical flux at the PTn-TSw interface becomes very large along the faults (the right boundary is also a fault). Note that there is one vertical fast flow path, at an Easting coordinate of about 172100 m in the profile (between Drill Hole Wash fault and Pagany Wash fault), that is

not caused by a fault (Figures 12 and 13). In this area, the thickness of PTn21 and PTn23 reduces to a critical value (below 2 m) and the dipping angle of the layer interfaces also reduces significantly (Figure 3). As a result, a “bottleneck” to the lateral flow formed in this area because the lateral flow is confined within PTn21 and PTn23, which causes the building up of water pressure and breaking down of the capillary barriers. The fast vertical flow path formed due to this mechanism smears wider in the way down than those along the faults (Figures 12 and 13) because of no vertical barrier that confines the fast flow path. This phenomenon is shown more clearly in the N-S cross section (Figure 14). Especially in the south part, both capillary diversion and focusing of percolation flow take place in a much small scale because the critical layers (e.g., PTn21) become less continuous and the dipping angle is much smaller. Even in the north part, the capillary diversion of flow takes place in the similar scale, but the leaking area becomes much wider and the flow focusing effect is less significant than what we have seen in the east-west cross section, except near the Drill Hole Wash fault. The reason is that the critical layers become thinner and the dipping angle becomes smaller gradually to the south (Figure 4).

Fractures and matrix have different responses to the same ambient flow condition, which increases the complicity of a capillary barrier in a vadose zone of fractured porous rocks. As shown in the analytical analyses, the fractures are critical in keeping the thick unsaturated zone in Yucca Mountain, by fast transmitting most of percolation flux to the water table, under the current average infiltration rate of 5 mm/yr. The numerical simulations provide additional information about the roles of the fractures in forming and

destroying the capillary barriers, because the numerical methods are not limited by the assumption of the equilibrium in the capillary pressure between fractures and matrix. Figure 15 shows a typical profile of the simulated vertical capillary pressure gradient in fractures and matrix corresponding to the steady-state ambient infiltration (extracted from the 2-D cross section simulation). Interestingly, the fracture capillary gradients are downward near the bottom of layer PTn21 while the matrix capillary gradients are upward in the entire PTn21 (Figure 15, positive downward), partly because the fracture hydraulic conductivity of PTn22 is larger than that of PTn21 for almost the entire range of the water pressure. This implies that a counter capillary force acts on the PTn21/PTn22 interface. For the given ambient infiltration condition, the effective hydraulic conductivity in the fractures of PTn21 is much smaller than that in the matrix. Therefore, the PTn21/PTn22 combination still acts as a capillary barrier to the downward flow but with some leakage in the fractures. However, at the intersection with vertical barriers (e.g., faults), such leakage can be big enough to destroy the capillary barrier of PTn21/PTn22 before the barrier in matrix completely diminished because the fractures become more important as the water pressure increases. On the other hand, the value of fracture hydraulic conductivity of PTn24 is similar to that of PTn23 except near fully saturated area. As a result, similar phenomenon does not occur and the capillary gradient is consistent with each other in both the fractures and the matrix of PTn23.

Flow diversion and focusing in real world is a 3-D phenomenon. A full 3-D numerical model of the unsaturated zone in Yucca Mountain with a refined grid (over a million grid cells) was built to investigate the big picture of the flow diversion and focusing in Yucca

Mountain unsaturated zone (Figure 8). Figure 16 shows the maps of the vertical downward flux at the bedrock surface, the repository level, and the water table, respectively, corresponding to the present day, mean infiltration. As shown in Figure 16a, the net infiltration rate at the bedrock surface is mainly controlled by the landscape in this desert mountain. A near-zero infiltration rate composes the background for the region while the high infiltration rate (up to more than 3 times of the mean infiltration rate) distributes along the directions of ridges and is concentrated in the northern part. At the repository level (below PTns), the background percolation rate slightly increases due to normal lateral diffusion of the moisture, especially in the northern part (Figure 16b). Remarkably, the high percolation areas have significantly shifted laterally and tend to focus into the fault zones because of the capillary barriers in PTns and the faults. The flow diversion and focusing processes continued below the repository level that can be seen by comparing Figure 16b and 16c. However, the processes below the repository level seem to be stronger in the southern part than in the northern part, which is consistent with the analytical solutions, because the layers below repository level (e.g., CH1/CH2) plays an important role in the southern part only (strictly say in the vitric zone). Consistent with the dipping directions of the critical layer contacts, the infiltration flow diverts to the east in the southern part and to the southeast in the northern part. Almost all of such diversion flow is stopped by the faults and fast flow paths are established along those faults. For those faults that are almost parallel to the diversion flow direction (e.g., Drill Hole Wash fault, Pageny Wash fault, and Sever Wash fault), the flow focusing zones are centered in the faults (Figure 16b and 16c). For those faults that are almost perpendicular to the flow diversion direction (e.g., Ghost Dance fault,

Sundance fault, etc.), the flow focusing zones are often established along the western walls of the faults (up-slope side). This difference implies that the faults like Ghost Dance fault act more as the vertical barriers than the faults like Drill Hole Wash fault do while the latter also act as fast paths for lateral flow because of their intersection angle with the diversion flow.

There are special points regarding the flow diversion and focusing in the area between the Solitario Canyon fault and the Ghost Dance fault in the southern part. The narrow, north-south trend, high infiltration zone along the east of the Solitario Canyon fault on the bedrock surface (Figure 16a) shifted to the Ghost Dance (west) fault with a shorter length (consistent with the length of the fault) at the water table. But such shifting only completed partly at the repository level because the critical layer PTn23 is pinched out in this area. In the north of the Ghost Dance (west) fault, a medium to high percolation area formed (Figures 16b and 16c). Different from the other area where the high percolation zones concentrated along the faults, many small, but above-background percolation zones combined into a region with a complicated percolation pattern. The reason is that this area is corresponding to a transition zone where the PTns starts to become thinner or pinched out, the dipping angle becomes flat (PTns) or reversed (the layers below PTn) as shown in Figure 4. All of these could cause a wide leaking zone of the capillary barrier as shown in Figure 14, even though it is weaker in the 3-D model than in the 2-D model. Note that, however, the flow diversion to the east is still significant as proven by the existing of high percolation zones along the Ghost Dance fault and the Ghost Dance (west) fault. Therefore, these factors or spatial variability cause the leaking of the

capillary barriers and reduce the flow diversion but not diminish them. As a counterpart, the faults often completely stop the lateral diversion flow that tends to cross them. Interestingly, the leaking downward flow between the Drill Hole Wash fault and the Pagany Wash fault revealed by 2-D analysis (Figure 12) is not significant at the repository level and disappears at the water table level in the 3-D model.

In the relatively dry southeast area (Figure 16a), a focused downward flow zone establishes along the east boundary at the water table level (Figure 16c). This zone, however, does not exist at the repository level (Figure 16b). Instead, the focused downward flow zone along the southern portion of the “imbricate” fault at the repository level (Figure 16b) almost disappears at the water table level (Figure 16c). These phenomena imply (1) that the large-scale diversion flow can take place underneath an area with little surface infiltration, resulting in a local high percolation sub-region and (2) that the focused downward flow along the fault could also be diverted to some significant distance.

5. Concluding Remarks

We have presented a systematic modeling study of flow diversion and focusing due to capillary barriers in the unsaturated zone of Yucca Mountain under ambient condition. The flow pattern in the Yucca Mountain unsaturated zone is a very complicated, 3-D phenomenon. Although the net infiltration rate at the bedrock surface depends on the landscape, the percolation flow through the thick unsaturated zone is mainly controlled

by a few of critical layers and faults. Among these critical layers, PTn21, PTn23, and vitric CH1 are the layers that conduct the most down-dip diversion flow while PTn22, PTn24, and vitric CH2 are the layers that act as capillary barriers to the downward percolation flux. Using an infinite long and parallel layers with a dipping angle of 10 degrees, our analytical analyses indicate that a total of diversion length of the unsaturated zone could be more than 1300 m responding to an infiltration rate of 5 mm/yr. However, if the infiltration rate increases to 1000 mm/yr, the diversion length may reduce to about 100 m or less. Meanwhile, the relative importance of the critical layers also changes as the infiltration rate changes. The layer combination TSw31/TSw32, for example, becomes the major contributor to the capillary diversion flow in the UZ-14 profile under wet or high-infiltration conditions.

The downward percolation is usually diverted toward east (southern part) or southeast (northern part) following the dipping direction of those critical layer contacts. Most faults or fault zones act as vertical barriers to the diversion flow and fast paths for the focused downward flow. In general, the focused flow zones form along the west walls of the faults that are perpendicular to the lateral diversion flow and along the center of the faults that parallel to the lateral diversion flow. In some local regions, the focused downward flow along the faults can be diverted again to a significant distance. The spatial distribution of the downward flux is greatly changed in depth due to the flow diversion and focusing processes caused by the complicated capillary-barrier effects in the Yucca Mountain. Remarkably, the downward flow tends to focus along the faults.

The diversion flow is usually confined within the higher hydraulic conductivity layers by the lower hydraulic conductivity layers right above and below those layers at the capillary pressure corresponding to the given local percolation conditions. Any spatial variability in the layer thickness, the dipping angles, and even the hydraulic properties of the same layer could cause leaking of, or even total fail of the capillary barriers.

According to the 3-D modeling, there is such a leaking area between the Solitario Canyon fault and the Ghost Dance fault in the Yucca Mountain. However, existence of the leaking area does not diminish the capillary-barrier diversion completely in that area as evidenced that the high downward flow zones still form along the Ghost Dance fault, the Ghost Dance (west) fault, and the Sundance fault.

Fractures play important roles in the flow diversion and focusing processes in the Yucca Mountain in many ways. Analytical analysis shows that the thick unsaturated zone in the Yucca Mountain might not exist without fractures providing pathways of the present-day infiltration at rate of 5 mm/yr. The water pressure gradient can also be different in the fractures and the matrix, even resulting in local counter flow in two media. This provides an additional mechanism that causes leaking of the capillary barrier even though we have not found any significant impacts in this steady-state analysis. However, it is expected that this mechanism may play a more important role in the flow diversion and focusing under condition of episodic infiltration events.

Reference

- Clayton, R.W., Geologic Framework Model (GFM3.1), *Report: MDL-NBS-GS-000002 REV 00 ICN 01*, Las Vegas, Nevada, CRWMS M&O, 2000.
- Day, W. C., C. J. Potter, D. E. Sweetkind, R. P. Dickerson and C. A. San Juan, Bedrock geologic map of the central block area, Yucca Mountain, Nye County, Nevada, Map I-2601, U.S. Geological Survey, 1998.
- Fayer, M.J., M.L. Rockhold, and M.D. Campbell, Hydrologic modeling of protecting barriers: comparison of field data and simulation results, *Soil Sci. Soc. Am. J.*, 56:690-700, 1992.
- Flint, L. E., Characterization of hydrogeologic units using matrix properties, Yucca Mountain, Nevada, *U.S. Geological Survey Water-Resources Investigations Report 97-4243*, 1998.
- Hinds, J. and L. H. Pan, Development of numerical grids for UZ flow and transport modeling, *Report ANL-NBS-HS-000015 REV 00*, Lawrence Berkeley National Laboratory, CRWMS M&O, 2000.
- Ho, C. K. and S. W. Webb, Capillary Barrier performance in heterogeneous porous media, *Water Resources Research*, 34(4), 603–609, 1998.
- Liu, H. H., C. Doughty, and G. S. Bodvarsson, An active fracture model for unsaturated flow and transport in fractured rocks, *Water Resource Research*, 34, 2633–2646, 1998.
- Miyazaki, T., Water flow in unsaturated soil in layered slopes, *Journal of Hydrology*, 102, 201–214, 1988.
- Montazer, P., and Wilson, W. E., *Conceptual Hydrologic Model of Flow in the Unsaturated Zone, Yucca Mountain, Nevada*. U.S. Geological Survey Water-Resources Investigations Report 84-4345, 1984.
- Morel-Seytoux and J. R. Nimmo, Soil water retention and maximum capillary drive from saturation to oven dryness, *Water Resources Research*, 35(7), 2031–2041, 1999.
- Morel-seytoux, H. J., P. D. Meyey, M. Nachabe, J. Touma, M. T. van Genuchten, and R. J. Lenhard, Parameter equivalence for the Brooks-Corey and van Genuchten soil characteristics: Preserving the effective capillary drive, *Water Resources Research*, 32(5), 1251–1258, 1996.
- Moyer, T. C., J. K. Geslin and L. E. Flint, Stratigraphic Relations and Hydrologic Properties of the Paintbrush Tuff Nonwelded (PTn) Hydrologic Unit, Yucca Mountain, Nevada, *U.S. Geological Survey Open File Rep. 95-397*, 1996.

- Oldenburg, C. M. and K. Pruess, On numerical modeling of capillary barriers, *Water Resources Research*, 29 (4), 1045–1056, 1993.
- Pan, L., A. W. Warrick and P. J. Wierenga, Downward water flow through sloping layers in the vadose zone: Time-dependence and effects of slope length, *Journal of Hydrology*, 199, 36–52, 1997.
- Philip, J. R., Hillslope infiltration: planar slopes, *Water Resources Research*, 27, 109–117, 1991.
- Pruess, K., TOUGH2-A General-Purpose Numerical Simulator for Multiphase Fluid and Heat Flow, *LBL-29400*, Lawrence Berkeley Laboratory, 1991.
- Ross B., The diversion capacity of capillary barriers, *Water Resources Research*, 26(5), 2625–2629, 1990.
- Ross, B., Reply, *Water Resources Research*, 27, 2157, 1991.
- Rulon, J., G. S. Bodvarsson and P. Montazer, Preliminary numerical simulations of groundwater flow in the unsaturated zone, Yucca Mountain, Nevada. *LBL-20553*, Lawrence Berkeley Laboratory, 1986.
- Steenhuis, T.S., Parlange, J.-Y. and Kung, K.-J.S., Comment on “The diversion capacity of capillary barriers” by Benjamin Ross, *Water Resources Research*, 27, 2155-2156, 1991.
- Stormont, J.C., The effect of constant anisotropy on capillary barrier performance, *Water Resources Research*, 31:783-785, 1995.
- van Genuchten, M. Th., 1980. A closed-form equation for predicting the hydraulic conductivity of unsaturated soils, *Soil Sci. Soc. Amer. J.*, 44(5), 892–898.
- Warren, J. E. and P. J. Root, The behavior of naturally fractured reservoirs, *Soc. Pet. Eng. J., Transactions, AIME*, 228, 245–255, 1963.
- Warrick, A. W., P. J. Wierenga and L. Pan, Downward water flow through sloping layers in the vadose zone: analytical solutions for diversions, *Journal of Hydrology*, 192, 321–337, 1997.
- Webb, S. W., Generation of Ross’ tilted capillary barriers division formula for different two-phase characteristic curves, *Water Resources Research*, 33(8), 1855–1859, 1997.

Wilson, M. L., Lateral Diversion in the PTn Unit: Capillary-barrier analysis, paper presented at *the 1996 International High Level Radioactive Waste Management Conference*, American Society of Civil Engineering, Las Vegas, Nevada, 1996.

Wittwer, C., G. Chen, G. S. Bodvarsson, M. Chornack, A. Flint, L. Flint, E. Kwicklis and R. Spengler, *Preliminary development of the LBL/usgs three-dimensional site-scale model of Yucca Mountain, Nevada*, LBL-37356, Lawrence Berkeley Laboratory, 1995.

Wu, Y. S., J. Liu, T. Xu, C. Haukwa, W. Zhang, H. H. Liu, and C. F. Ahlers, UZ flow models and submodels, *Report MDL-NBS-HS-000006*, Lawrence Berkeley National Laboratory, CRWMS M&O, 2000.

Wu, Y. S., On the effective continuum method for modeling multiphase flow, multicomponent transport and heat transfer in fractured rock, “*Dynamics of Fluids in Fractured Rocks, Concepts and Recent Advances*”, Edited by B. Faybishenko, P. A. Witherspoon and S. M. Benson, **AGU Geophysical Monograph** 122, American Geophysical Union, Washington, DC, pp. 299-312, 2000.

Wu, Y. S., C. Haukwa and G. S. Bodvarsson, A site-scale model for fluid and heat flow in the unsaturated zone of Yucca Mountain, Nevada, *Journal of Contaminant Hydrology*. 38 (1-3), 185–217, 1999.

Wu, Y. S., A. C. Ritcey, C. F. Ahlers, J. J. Hinds, A. K. Mishra, C. Haukwa, H. H. Liu, E. L. Sonnenthal and G. S. Bodvarsson, 3-D UZ site-scale model for abstraction in TSPA-VA, *Yucca Mountain Project Level 4 Milestone Report SLX01LB3*, Lawrence Berkeley National Laboratory, 1998.

Wu, Y.-S., K. Zhang, C. Ding, K. Pruess, E. Elmroth, and G. S. Bodvarsson. An Efficient Parallel-Computing Scheme for Modeling Nonisothermal Multiphase Flow and Multicomponent Transport in Porous and Fractured Media. *Advances in Water Resources* 2001 (Submitted).

Yeh, T.-C., A. Guzman, R. Srivastava, and P.E. Gagnard, Numerical simulation of the wicking effect in liner systems, *Ground Water*, 32:2-11, 1994.

Acknowledgements

This work was supported by the Director, Office of Civilian Radioactive Waste Management, U.S. Department of Energy, through Memorandum Purchase Order EA9013MC5X between Bechtel SAIC Company, LLC and the Ernest Orlando Lawrence Berkeley National Laboratory (Berkeley Lab). The support is provided to Berkeley Lab through the U.S. Department of Energy Contract No. DE-AC03-76SF00098.

List of Tables

Table 1 Five most critical layers in the UZ-14 profile

Infiltration rate	Layer	Underlying layer	Qh (m ² /yr)	Contribution to the Total lateral flow (%)	Elevation of the contact (m)	Thickness (m)
5 mm/year	PTn23	PTn24	7.2385	88.32	1331.9	3.9
	PTn21	PTn22	0.9244	11.28	1341.2	1.9
	PTn25	PTn26	0.0461	0.56	1277.6	42.2
	Pp1	Bf3	-0.0214	-0.26	667.5	102.4
	TSw32	TSw33	0.0077	0.09	1218.8	43.8
1000 mm/year	TSw31	TSw32	41.2978	62.60	1262.6	2.0
	PTn23	PTn24	15.7808	23.92	1331.9	3.9
	PTn21	PTn22	6.1317	9.29	1341.2	1.9
	Pp3	Pp2	2.2562	3.42	784.8	10.7
	PTn25	PTn26	0.3276	0.50	1277.6	42.2

Table 2 Five most critical layers in the SD-12 profile

Infiltration rate	Layer	Underlying layer	Qh (m ² /yr)	Contribution to the Total lateral flow (%)	Elevation of the contact (m)	Thickness (m)
5 mm/year	PTn21	PTn22	3.0815	45.83	1243.3	2.4
	CH1	CH2	2.4612	36.60	893.5	22.5
	CH5	CH6	1.1550	17.18	836.2	14.3
	PTn25	PTn26	0.0351	0.52	1234.9	4.0
	Pp1	Bf3	-0.0212	-0.31	660.5	94.8
1000 mm/year	CH1	CH2	44.2476	41.85	893.5	22.5
	TSw31	TSw32	41.2978	39.06	1222.8	2.0
	PTn21	PTn22	12.4167	11.74	1243.3	2.4
	PTn22	PTn24	3.0877	2.92	1242.6	0.7
	Pp3	Pp2	2.2569	2.13	779	33.6

Table 3 The most critical layers in the UZ-14 and the SD-12 profiles without fractures corresponding to an infiltration rate of 5 mm/year

Profile	Layer	Underlying layer	Qh (m ² /yr)	Contribution to the Total lateral flow (%)	Elevation of the contact (m)	Thickness (m)
UZ-14	PTn22	PTn23	848.85	60.97	1335.8	5.4
	PTn25	PTn26	175.15	12.58	1277.6	42.2
	PTn26	TSw31	170.26	12.23	1264.6	13.0
	PTn21	PTn22	111.60	8.02	1341.2	1.9
	PTn24	PTn25	56.40	4.05	1319.8	12.1
SD-12	CH1	CH2	1321.48	64.31	893.5	22.5
	PTn21	PTn22	140.96	6.86	1243.3	2.4
	PTn26	TSw31	132.28	6.44	1224.8	10.1
	PTn22	PTn24	110.03	5.36	1242.6	0.7
	CH4	CH5	79.17	3.85	850.5	14.4

List of Figures

- Figure 1. Plan view of the UZ model domain, showing the model boundary, the potential repository outline, major fault locations from GFM 3.1, the paths of the ESF and ECRB, selected boreholes, and the location of cross sections used in the capillary-barrier modeling studies described in this paper.
- Figure 2. The map of net infiltration at the bedrock surface (present day, mean infiltration).
- Figure 3. Geological profile along cross section through borehole UZ-14, taken at a Northing coordinate of 235,087 meters.
- Figure 4. Geological profile along north-south cross section, taken at an Easting coordinate of 170,600 meters.
- Figure 5. The effective hydraulic conductivity (ECM) as a function of water pressure head in selected tuffs.
- Figure 6. 2-D vertical numerical grids for the east-west cross section through UZ-14 ($\Delta x = 10$ m, $\Delta z = 2 \sim 20$ m).
- Figure 7. 2-D vertical numerical grids for the north-south cross section ($\Delta x = 10$ m, $\Delta z = 2 \sim 4$ m).
- Figure 8. The map view of the 3-D site-scale grid (over 1 million grid cells).
- Figure 9. Calculated effective hydraulic conductivity in the UZ-14 profile corresponding to an infiltration rate of (a) 5 mm/yr and (b) 1000 mm/yr, respectively.
- Figure 10. Calculated effective hydraulic conductivity in the SD-12 profile corresponding to an infiltration rate of (a) 5 mm/yr and (b) 1000 mm/yr, respectively.
- Figure 11. Calculated distributions of water pressure head responding to an infiltration rate of 5 mm/yr in (a) UZ-14 profile and (b) SD-12 profile, respectively, assuming no fractures at all.
- Figure 12. Magnitude of simulated 2-D vectors of mass flux (kg/s/m^2) along the cross section through UZ-14 corresponding to a uniform surface net infiltration of 5 mm/yr.
- Figure 13. Simulated vertical percolation flux at the PTn-TSw interface along the cross section through UZ-14 corresponding to a uniform surface net infiltration of 5 mm/yr.

- Figure 14. Magnitude of simulated 2-D vectors of mass flux (kg/s/m^2) along the N-S cross section corresponding to a uniform surface net infiltration of 5 mm/yr.
- Figure 15. Simulated vertical capillary pressure gradients (bar/m) in the fractures and matrix, respectively.
- Figure 16. Simulated downward water flux at two different elevations corresponding to the present-day, mean infiltration rate. (a) the net infiltration at bedrock surface; (b) at repository level; (c) at water table level.

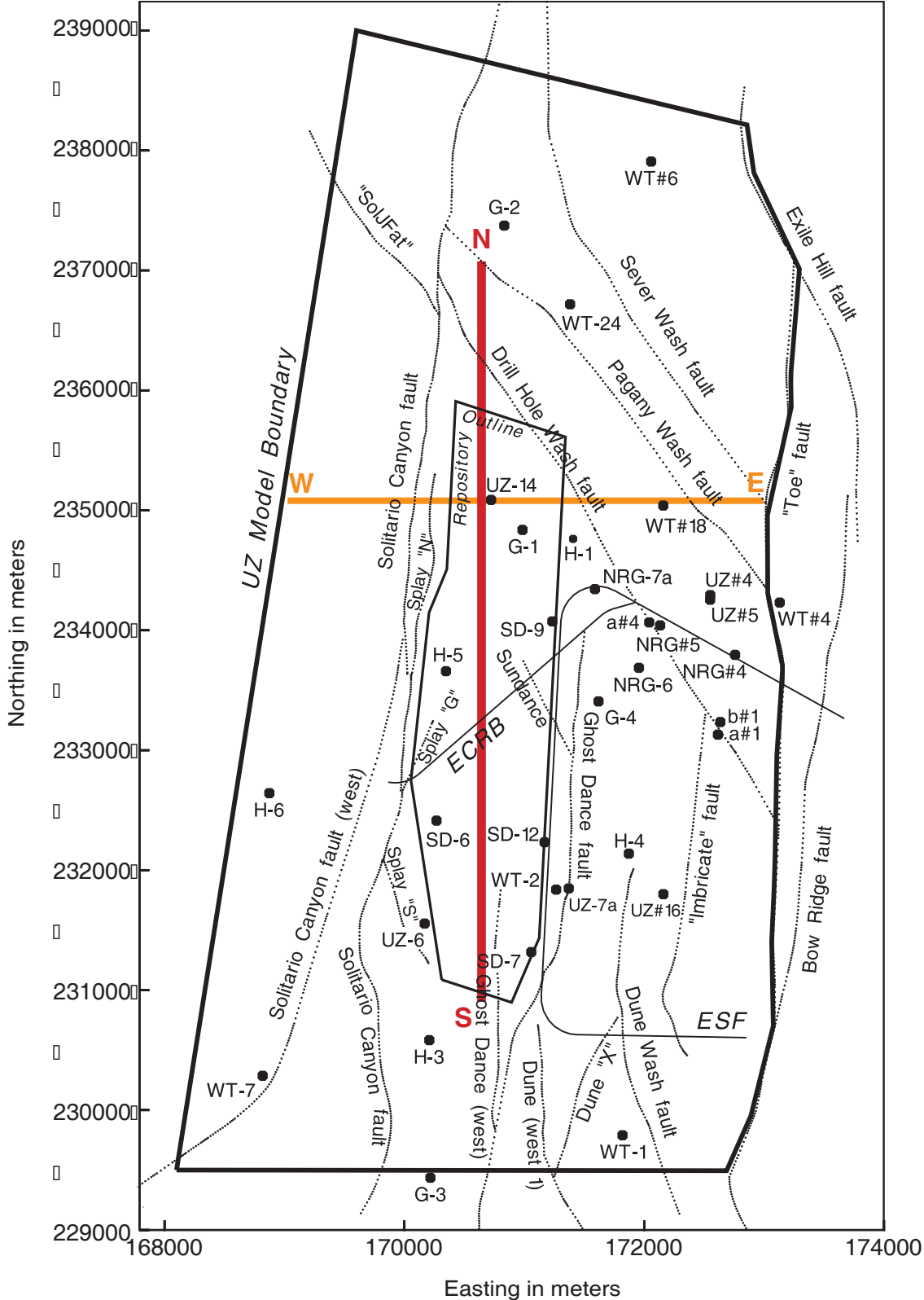
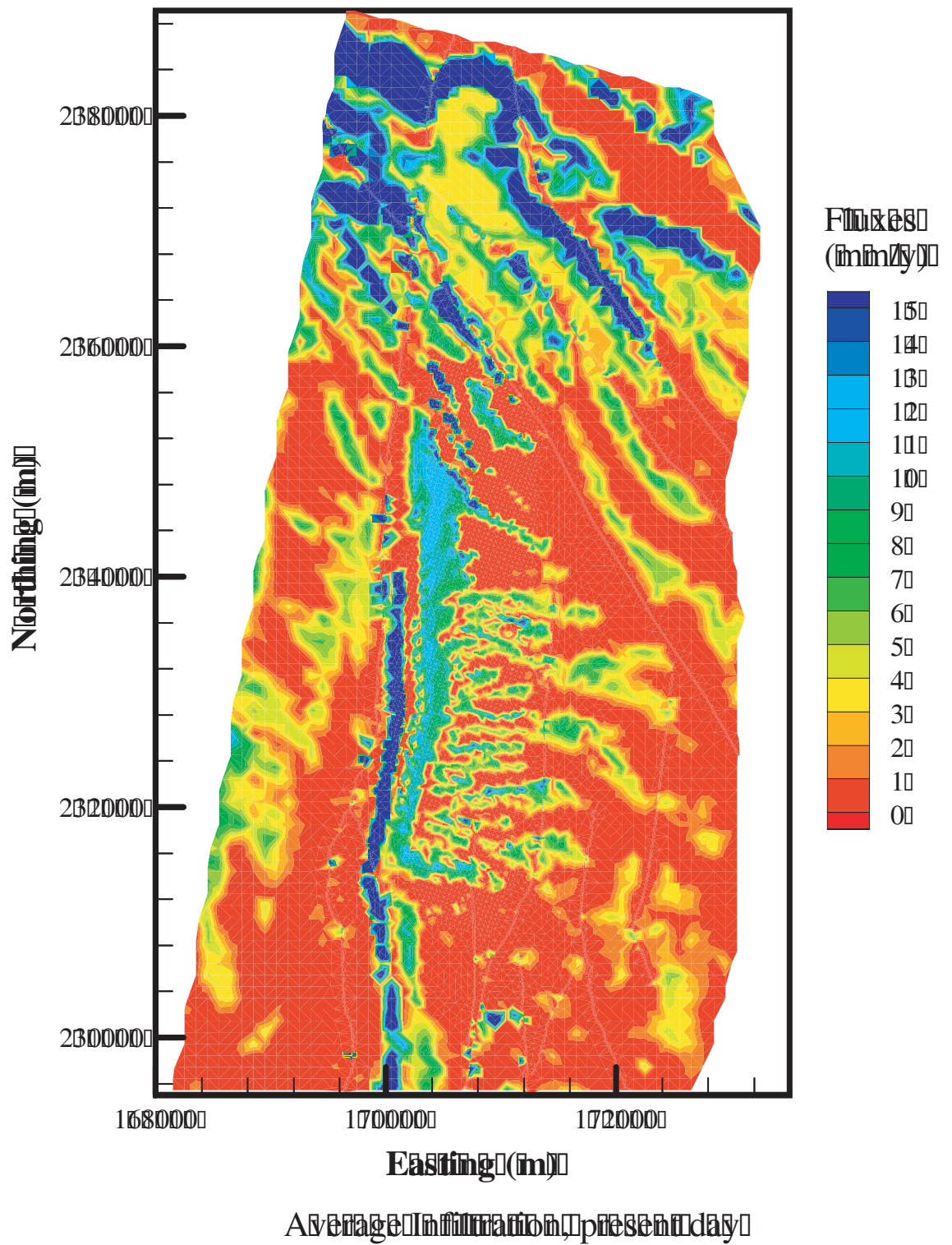


Figure 1. Plan view of the UZ model domain, showing the model boundary, the potential repository outline, major fault locations from GFM 3.1, the paths of the ESF and ECRB, selected boreholes, and the location of cross sections used in the capillary-barrier modeling studies described in this paper.



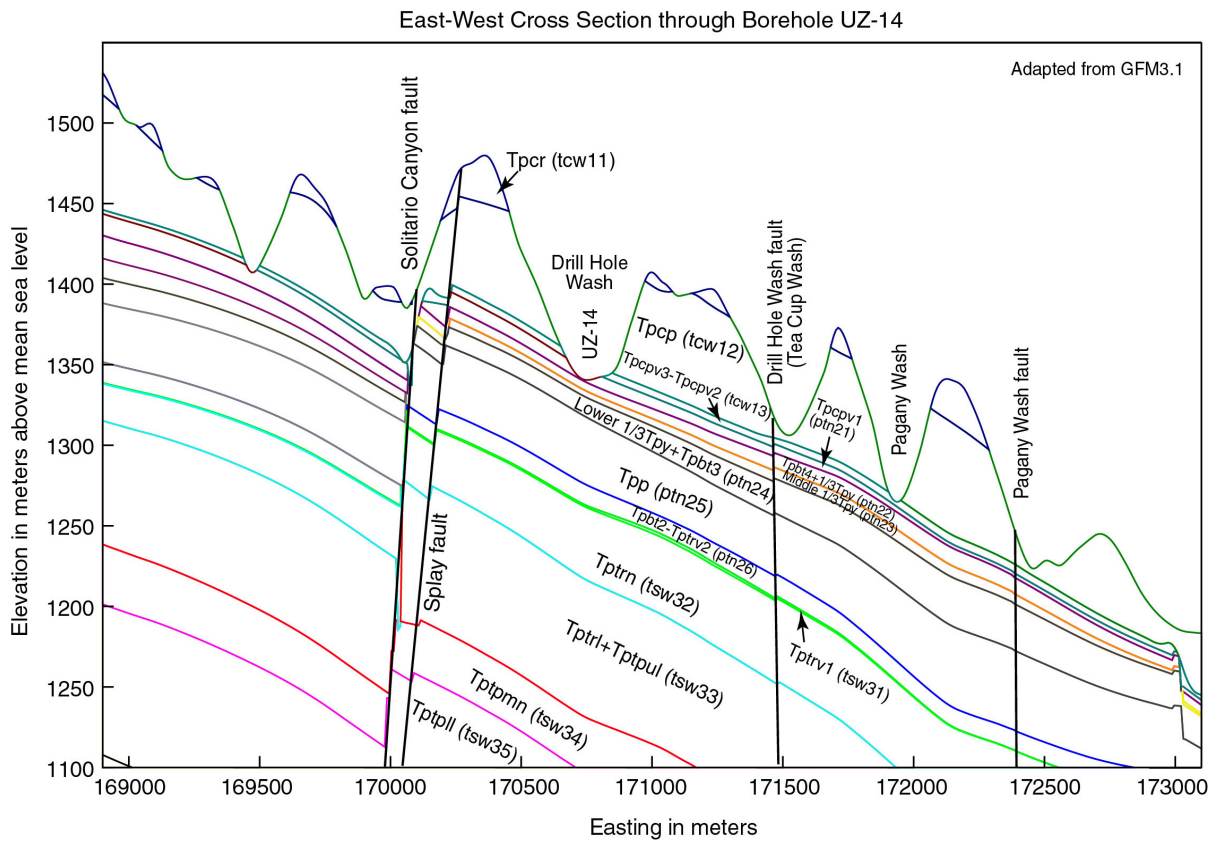


Figure 3. Geological profile along cross section through borehole UZ-14, taken at a Northing coordinate of 235,087 meters.

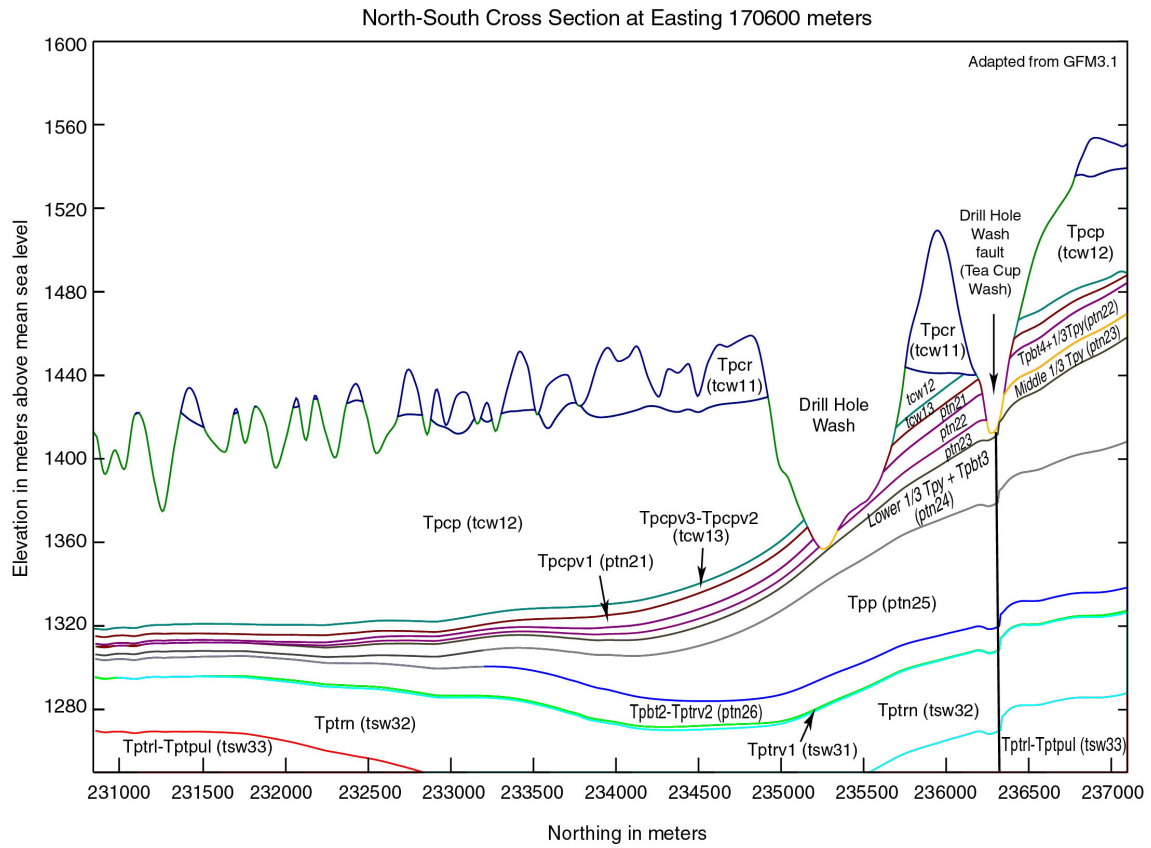


Figure 4. Geological profile along north-south cross section, taken at an Easting coordinate of 170,600 meters.

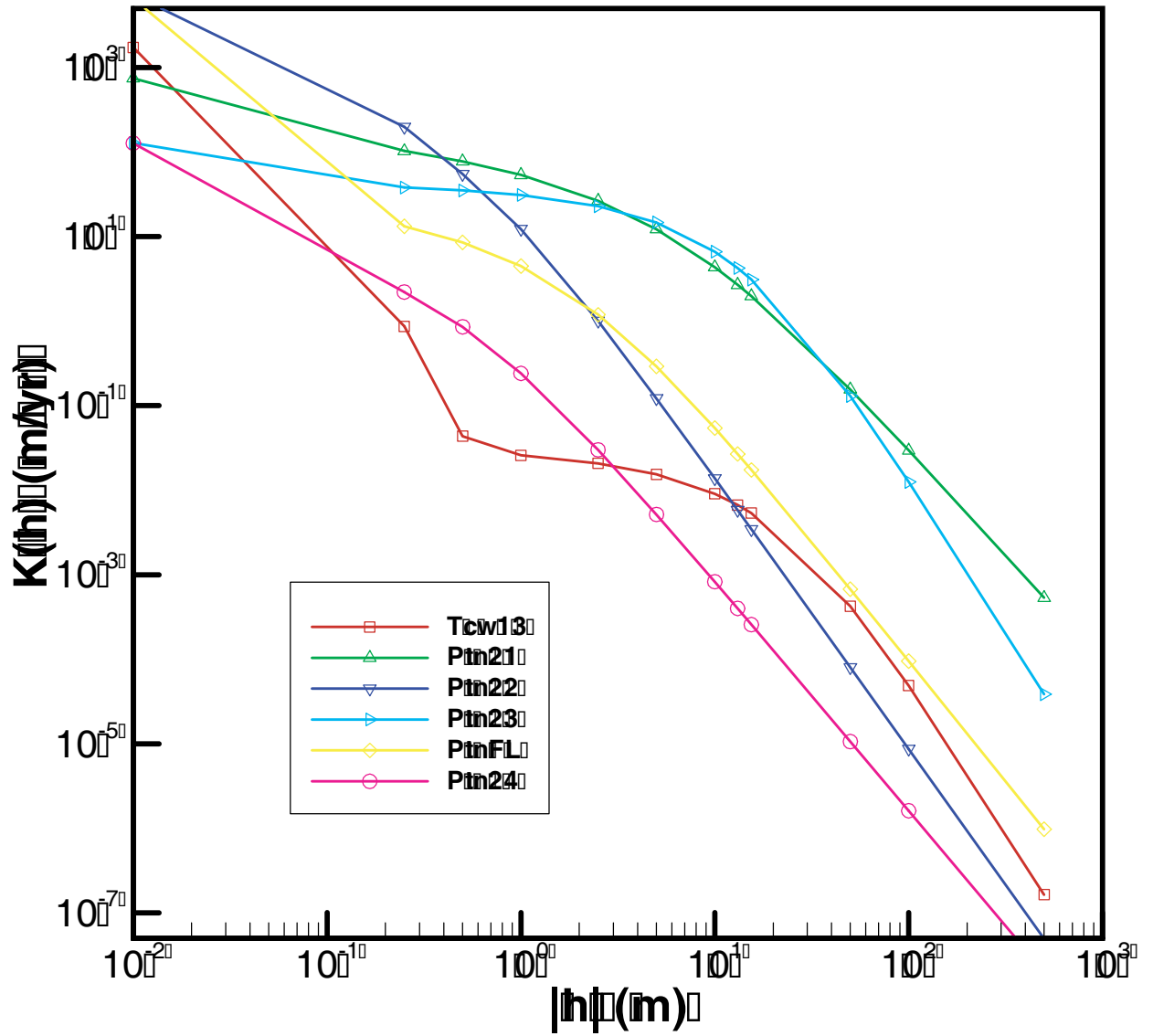


Figure 5. The effective hydraulic conductivity (ECM) as a function of water-pressure head in selected tuffs.

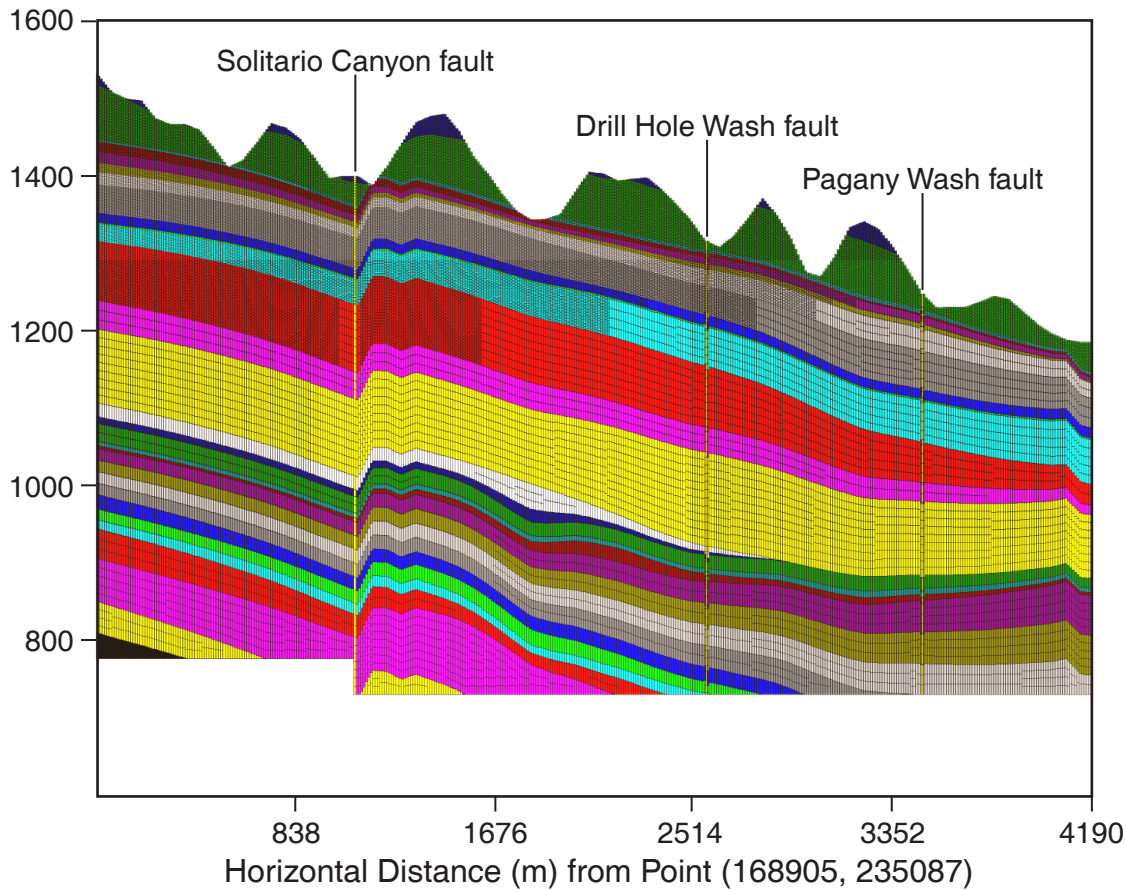


Figure 6. 2-D vertical numerical grids for the east-west cross section through UZ-14
 (Δx = 10 m, Δz = 2 ~ 20 m).

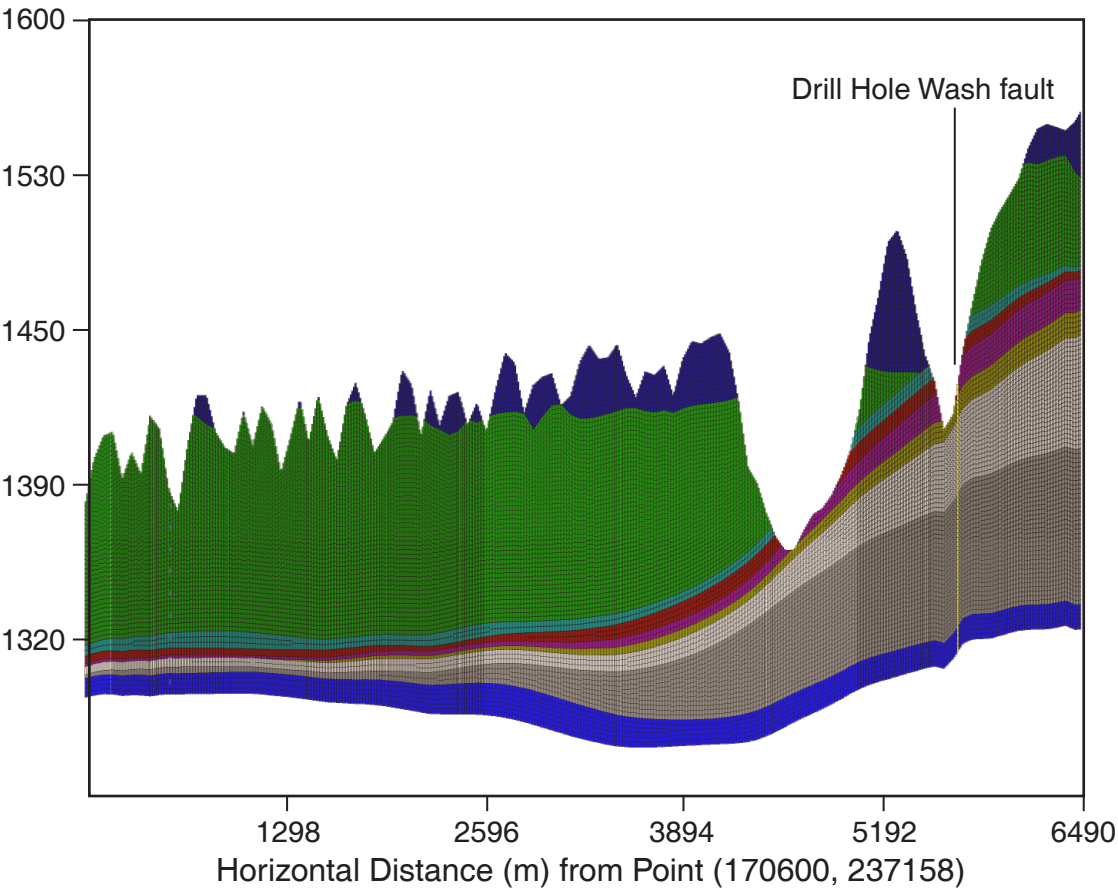


Figure 7. 2-D vertical numerical grids for the N-S cross section ($\Delta x = 10$ m, $\Delta z = 2 \sim 20$ m).

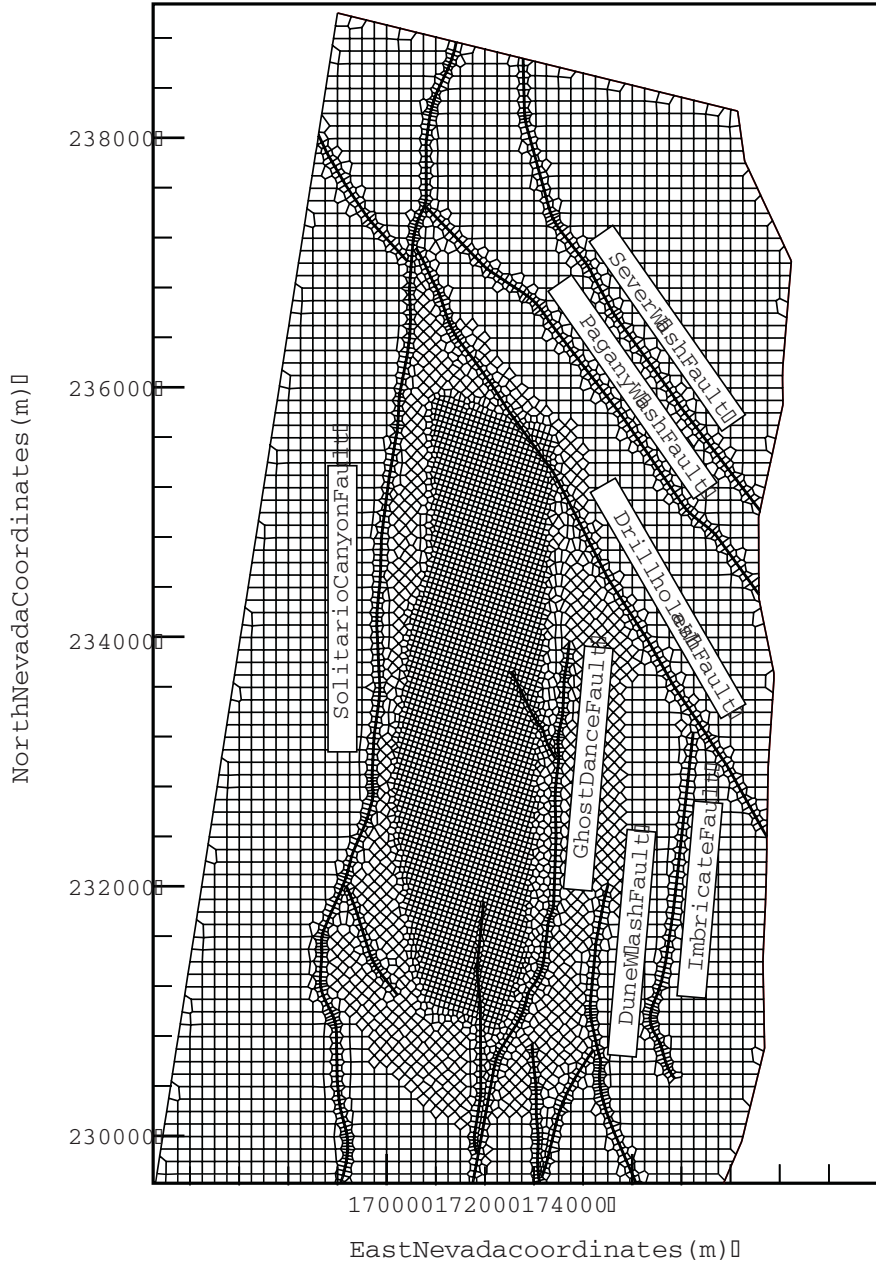
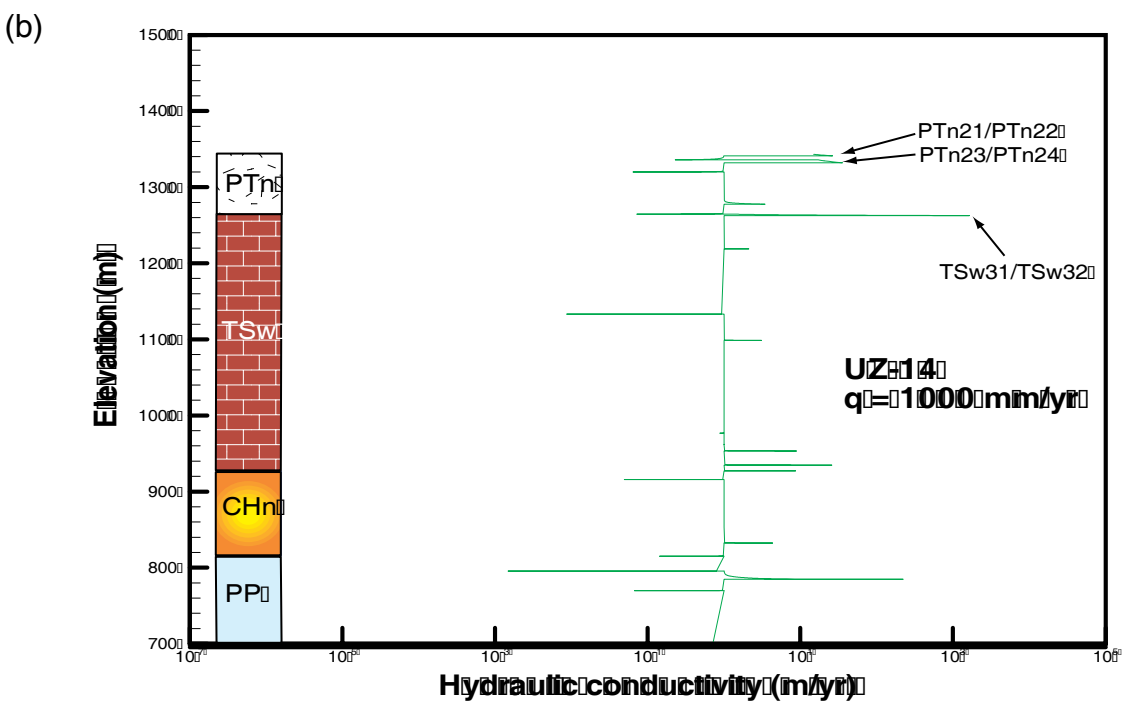
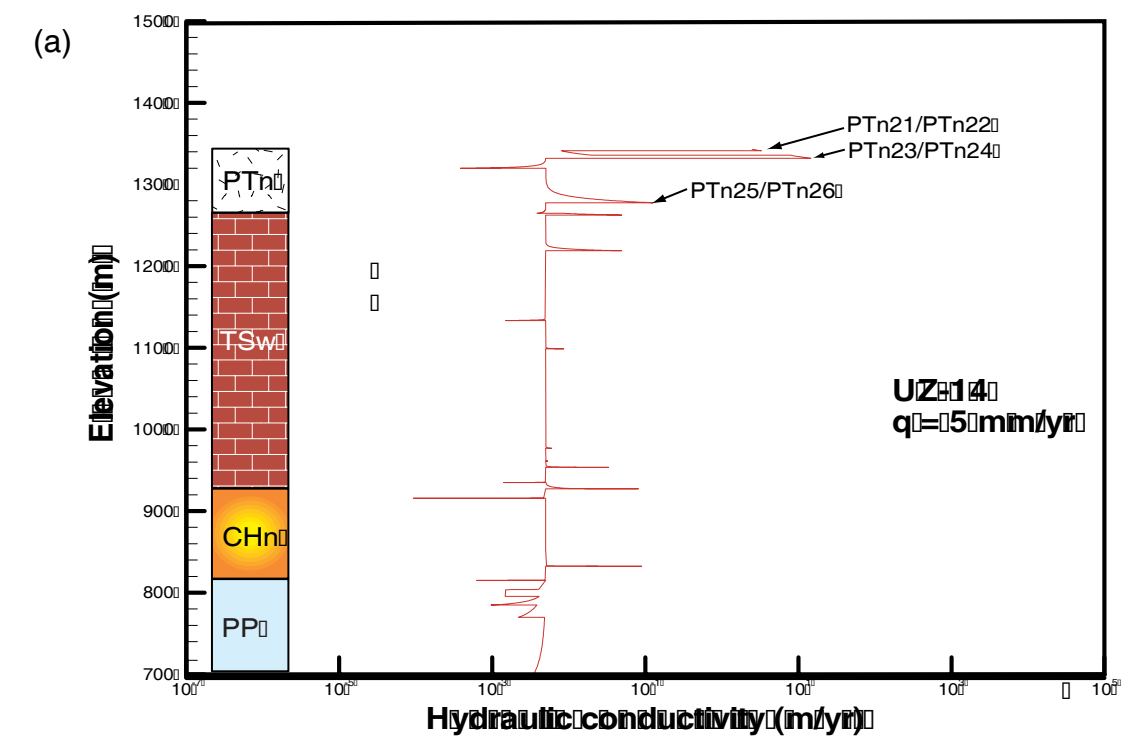
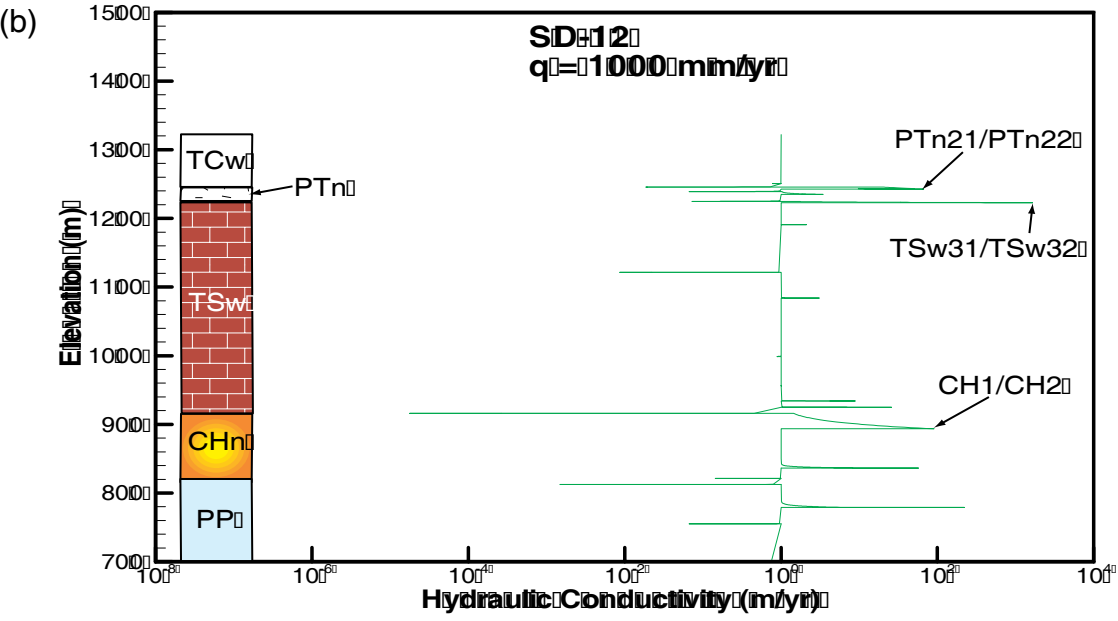
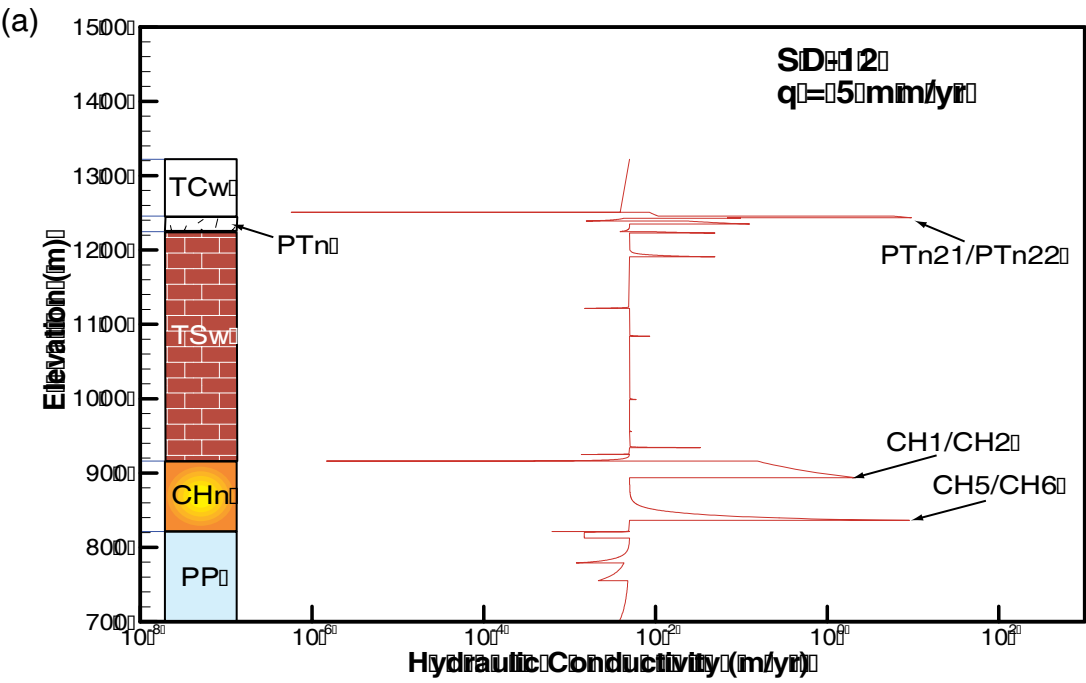


Figure 8. The map view of the 3-d site-scale grid (over 1 million grid cells).



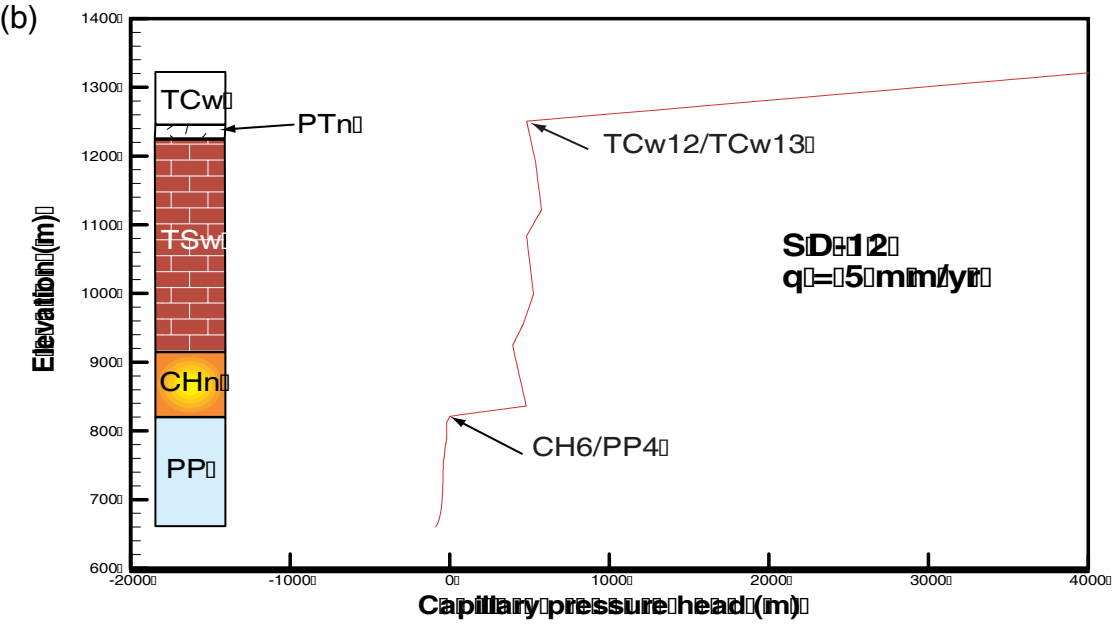
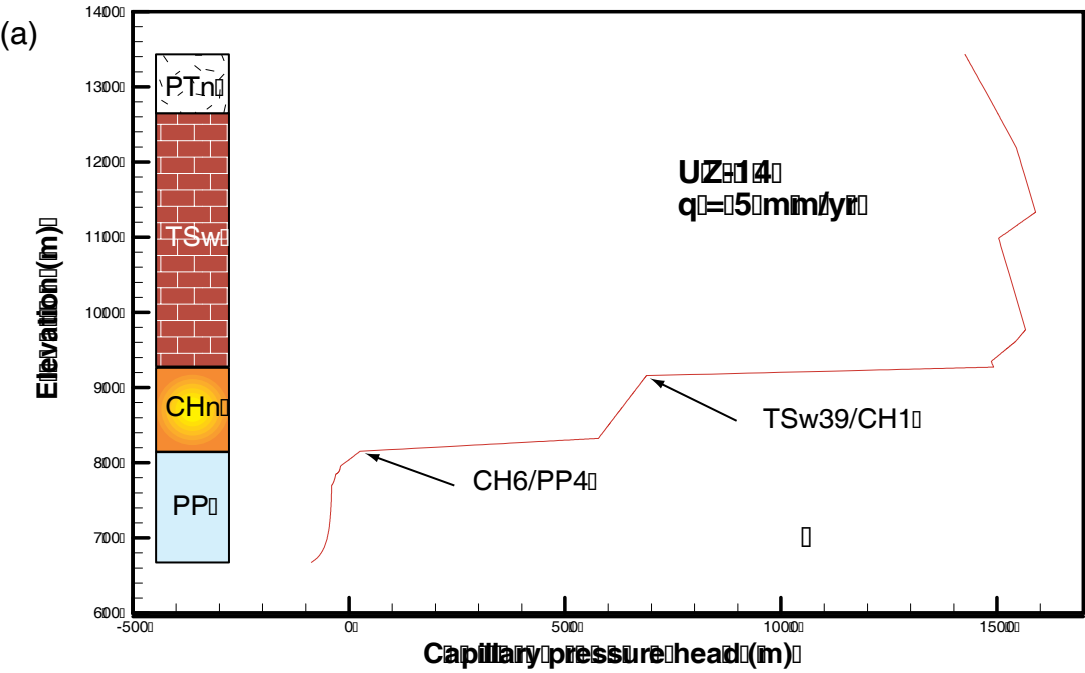
*PP -- Prow Pass

Figure 9. Calculated effective hydraulic conductivity in the UZ-14 profile corresponding to an infiltration rate of (a) 5 mm/yr and (b) 1000 mm/yr, respectively. The critical layer contacts are labeled.



* PP -- Prow Pass

Figure 10. Calculated effective hydraulic conductivity in the SD-12 profile corresponding to an infiltration rate of (a) 5 mm/yr and (b) 1000 mm/yr, respectively. The critical layer contacts are labeled.



*PP -- Prow Pass

Figure 11. Calculated distribution of water pressure head corresponding to an infiltration rate of 5 mm/yr in (a) UZ-14 profile and (b) SD-12 profile, respectively, assuming no fractures at all. The critical layer contacts are labeled.

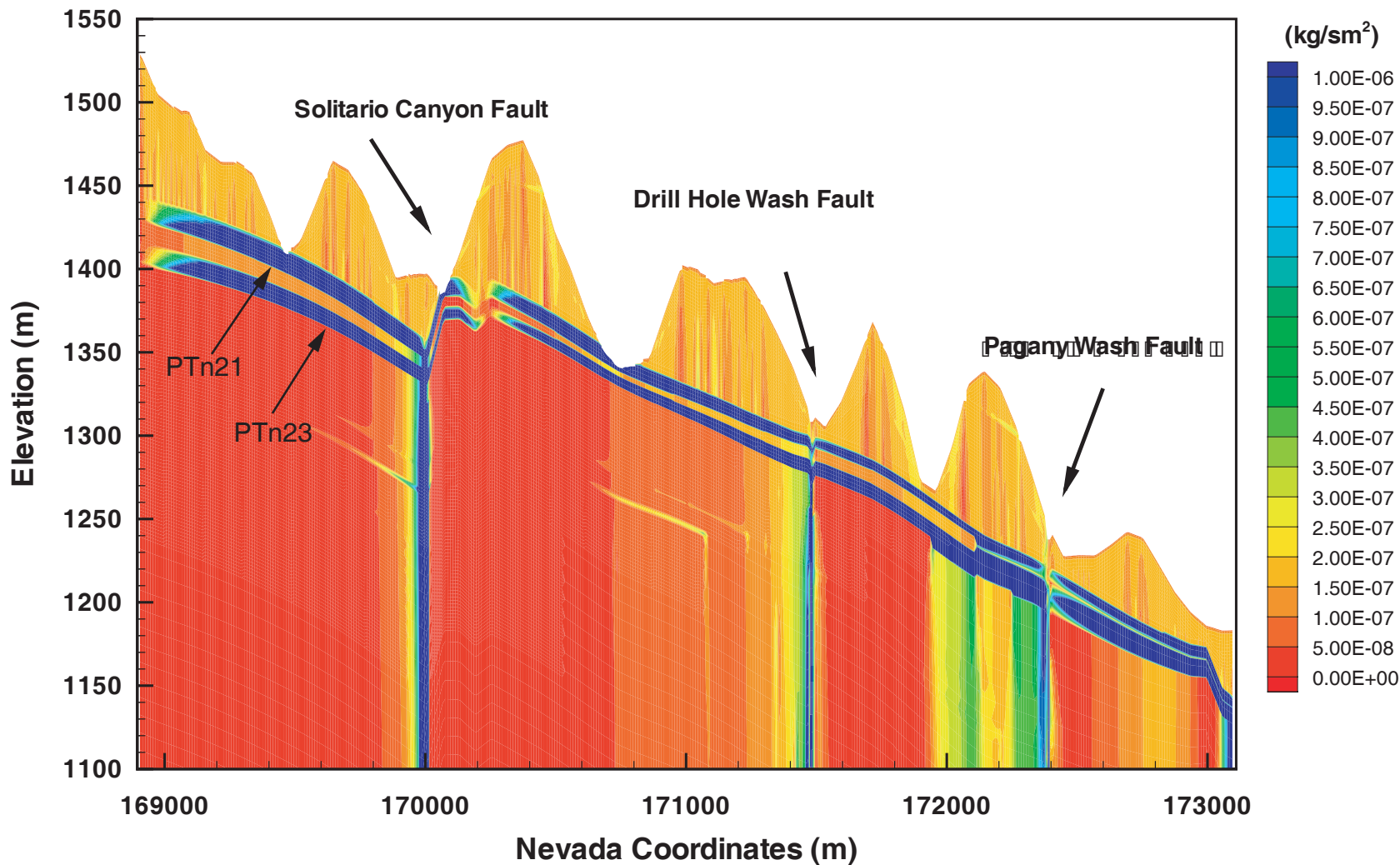


Figure 12. Magnitude of simulated 2-D vectors of mass flux (kg/s/m^2) along the cross section through UZ-14 corresponding to a uniform surface net infiltration of 5 mm/yr.

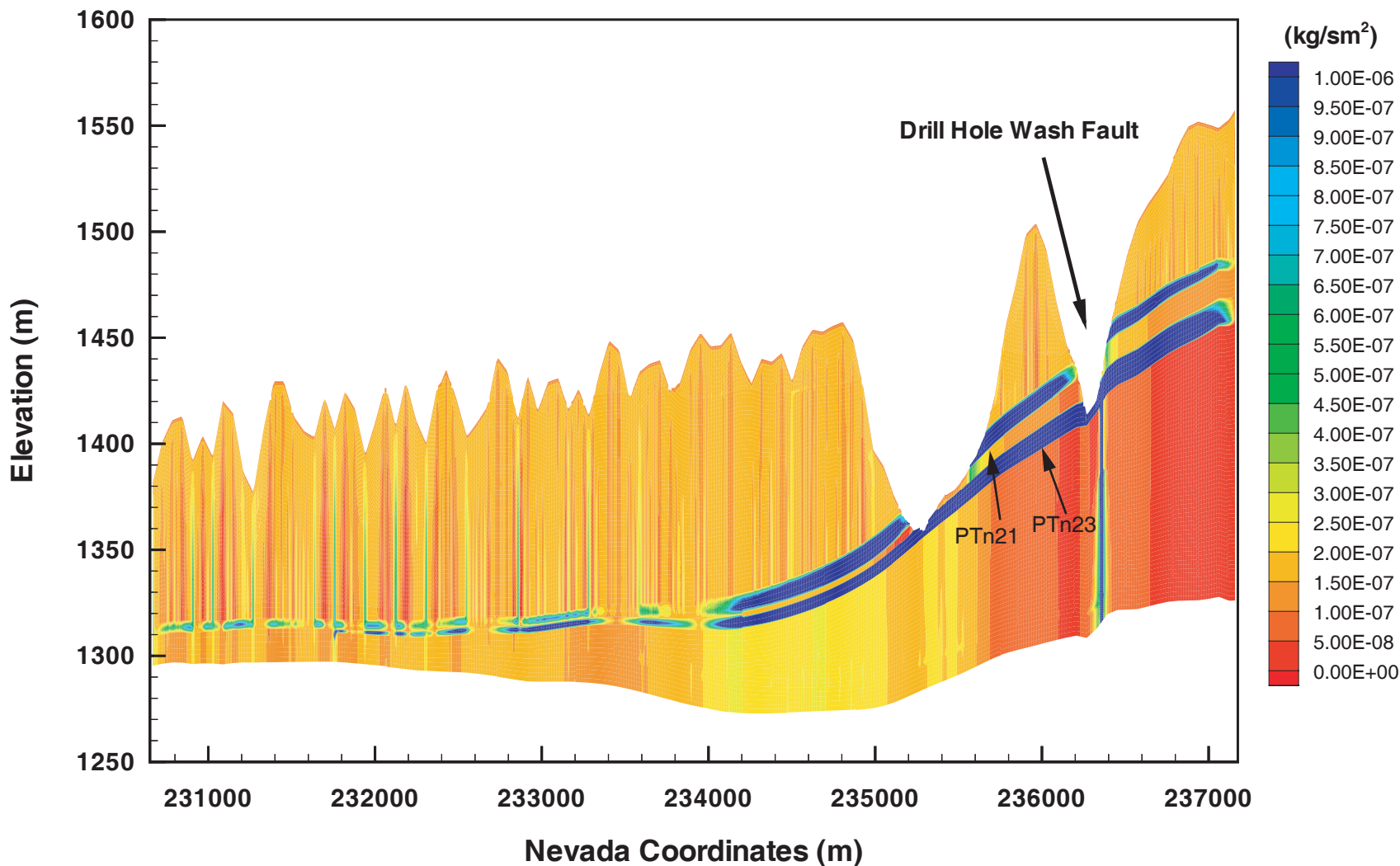


Figure 13. Magnitude of simulated 2-D vectors of mass flux (kg/s/m^2) along the N-S cross section corresponding to a uniform surface net infiltration of 5 mm/yr.

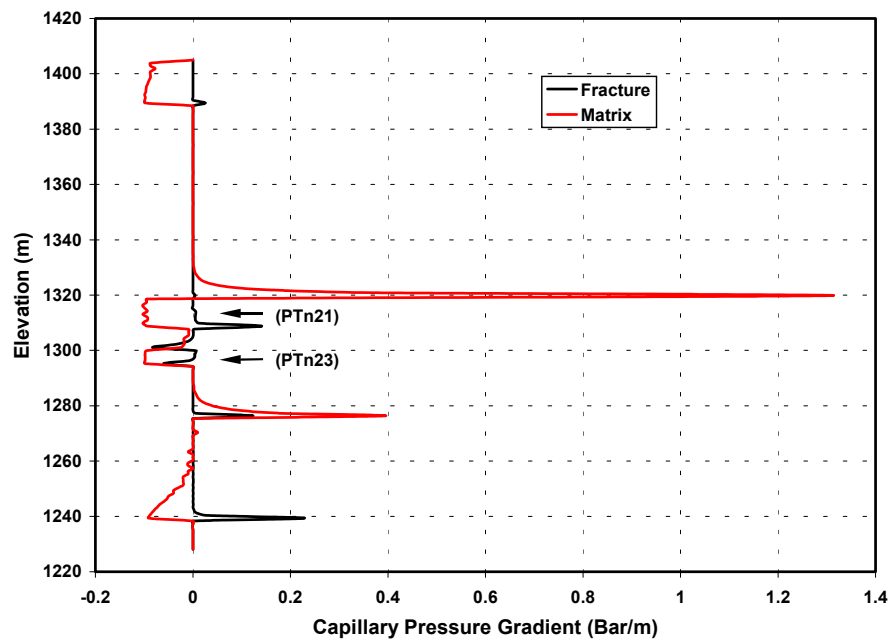


Figure 14. Simulated vertical capillary pressure gradients (bar/m) in the fractures and matrix, respectively.

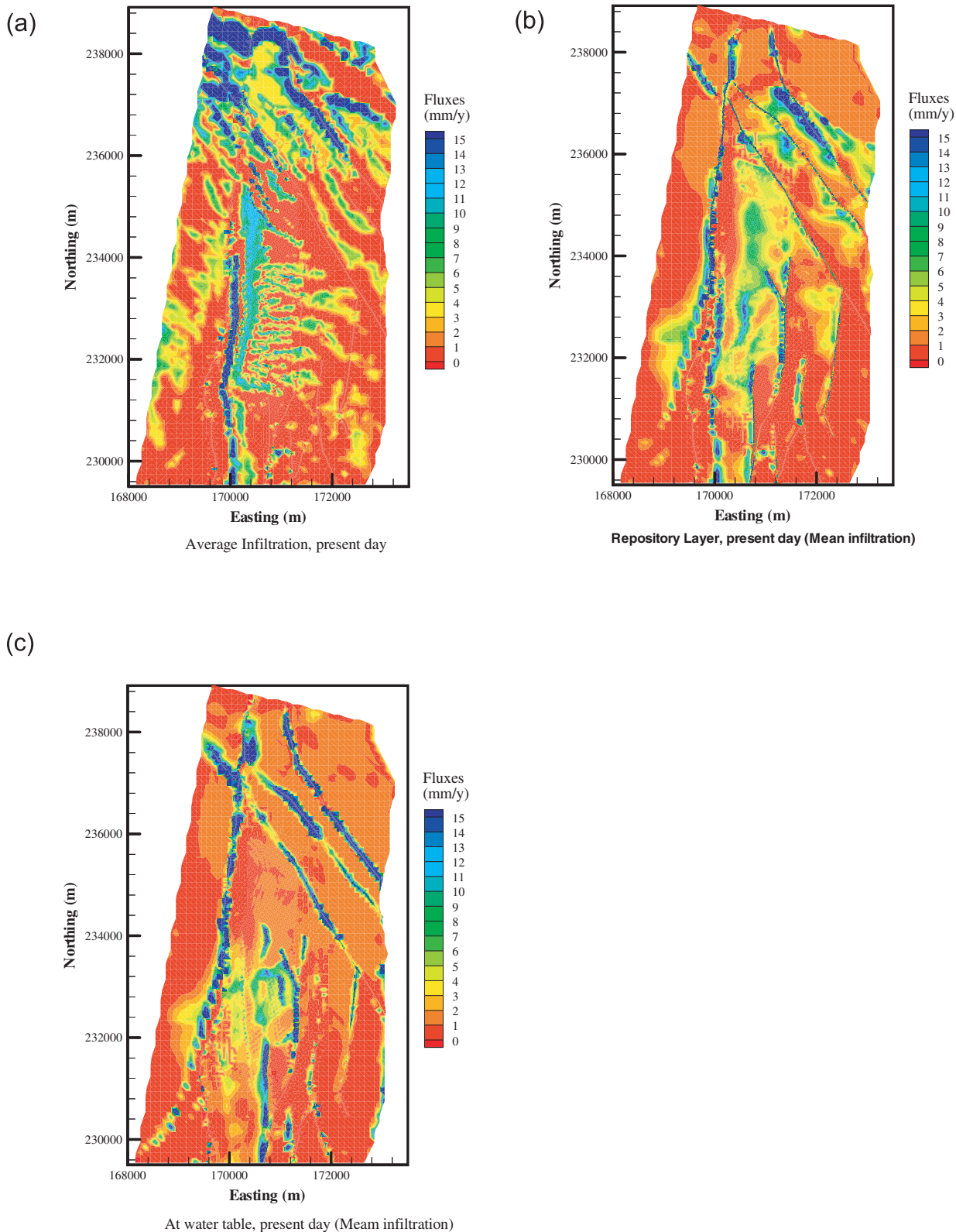


Figure 15. Simulated downward water flux at two different elevations corresponding to the present-day, mean infiltration rate. (a) at bedrock surface (input); (b) at repository level; (c) at water table level.